Degradation of lithium ion batteries employing graphite negatives and nickel–cobalt–manganese oxide + spinel manganese oxide positives: Part 1, aging mechanisms and life estimation

John Wang [a, *], Justin Purewal [a], Ping Liu [a], Jocelyn Hicks-Garner [a], Souren Soukazian [a],
Elena Sherman [a], Adam Sorenson [a], Luan Vu [a], Harshad Tataria [b], Mark W. Verbrugge [c]

[a] Sensors and Materials Lab, HRL Laboratories, LLC, Malibu, CA 90265, USA
[b] GM Vehicle Engineering, Global Battery Systems Engineering, Warren, MI 48092, USA
[c] GM R&D, Chemical and Materials Systems Lab, Warren, MI 48092, USA

HIGHLIGHTS

- We report on cycling-induced capacity fade in NCM + LMO/graphite Li-ion cells.
- Capacity loss is strongly affected by the rate, temperature, and depth of discharge.
- Lithium loss outpaces loss of active negative and positive electrode materials. .
- Calendar loss follows a square root of time relationship.
- Cycle loss is approximately linear as a function of charge throughput.

ARTICLE INFO

ABSTRACT

We examine the aging and degradation of graphite/composite metal oxide cells. Non-destructive electrochemical methods were used to monitor the capacity loss, voltage drop, resistance increase, lithium loss, and active material loss during the life testing. The cycle life results indicated that the capacity loss was strongly impacted by the rate, temperature, and depth of discharge (DOD). Lithium loss and active electrode material loss were studied by the differential voltage method; we find that lithium loss outpaces active material loss. A semi-empirical life model was established to account for both calendar-life loss and cycle-life loss. For the calendar-life equation, we adopt a square root of time relation to account for the diffusion limited capacity loss, and an Arrhenius correlation is used to capture the influence of temperature. For the cycle life, the dependence on rate is exponential while that for time (or charge throughput) is linear.

1. Introduction

Lithium ion batteries are now used in the automotive, commercial aircraft, and space industries. For vehicular applications, understanding battery life performance is important; not knowing a battery's useful life increases business risks and warranty costs. There have been extensive efforts focused on the development of battery life models to predict capacity fade in lithium ion batteries [1–12]. Different capacity fade models have been established based on the proposed aging mechanisms such as parasitic side reactions [7,8,13], SEI formation [11], and resistance increase [2,14]. However, experimental data are needed to understand the capacity fade and validate the aging mechanisms. Very often, a significant amount of testing is needed to develop a reliable model to account for multiple factors effecting battery life. Very few groups have attempted to develop a life prediction model using a large experimental data set. Bloom and Wright et al. [15–17], presented the testing and life modeling of lithium ion batteries with Ni-based lithium insertion cathodes including $LiNi_{0.8}Co_{0.2}O_2$ and $LiNi_{0.8}Co_{0.15}Al_{0.05}O_2$. Recently, we established cycle-life models of a graphite/LiFePO4 battery using a large cycle-test matrix [18]. These results have demonstrated the importance of using large test matrixes to evaluate and validate the life modeling of lithium ion batteries.

* Corresponding author. Tel.: +1 310 317 5155; fax: +1 310 317 5840.
E-mail address: jswang@hrl.com (J. Wang).

Manganese-based lithium ion batteries have been considered as a viable candidate for large scale energy storage systems such as vehicular applications. In particular, $[LiNi_{1/3}Co_{1/3}Mn_{1/3} + LiMn_2O_4]$ composite cathode electrodes promise a good balance of both energy density and power density [19–22]. $LiNi_{1/3}Co_{1/3}Mn_{1/3}$ provides very good energy storage capacity at 180 mAh g^{-1}, while $LiMn_2O_4$ offers excellent rate capabilities. However, capacity fade

behavior and life modeling for this battery has not been well established. Recently, Dubarry et al. [23,24], presented an insightful aging analysis of lithium ion battery comprising $[LiNi_{1/3}Co_{1/3}Mn_{1/3} + LiMn_2O_4]$ composite cathode using incremental capacity technique for the cell cycled at 2 C rate. In another report, Gering et al. [25], investigated the aging behavior of the same targeted chemistry cycled under specific vehicle duty cycle protocols. In this report, we further evaluate the aging mechanisms of a $LiNi_{1/3}Co_{1/3}Mn_{1/3} + LiMn_2O_4$ composite cathode cell under a wide range of temperatures, rates, and depth of discharge (DOD). The results agree with prior reports indicating that capacity fade is mainly caused by the loss of active lithium inventory.

This report focuses on understanding the aging mechanisms and developing a semi-empirical life model to account for both calendar life loss and cycle life loss using data collected from a large cycle-test matrix. Through the capacity data trend analysis and differential voltage analysis of the discharge profiles, we identify the aging behaviors of lithium ion batteries with $LiNi_{1/3}Co_{1/3}Mn_{1/3} + LiMn_2O_4$ composite cathode chemistry. We determine that there are two degradation mechanisms contributing to the lithium loss: 1) high rates at low temperature triggers accelerated lithium loss, perhaps due to excessive SEI formation of cycle-induced cracks on graphite particles, and 2) high temperatures cause accelerated calendar life loss, likely due to chemical side reactions that consume lithium.

Fig. 1. Test matrix for accelerated cycle life study. Two cells were tested at each condition. Colored highlights represents the selected test conditions: four temperatures (10 °C, 22 °C, 34 °C, 46 °C) five discharge currents (0.5 C, 2 C, 3.5 C, 5 C, 6.5 C) and five discharge depths (10%, 30%, 50%, 70%, 90%). Lines shown here are for the guidance of the data trend, not from model fit. (For interpretation of the references to color in this figure legend, the reader is referred to the web version of this article.)
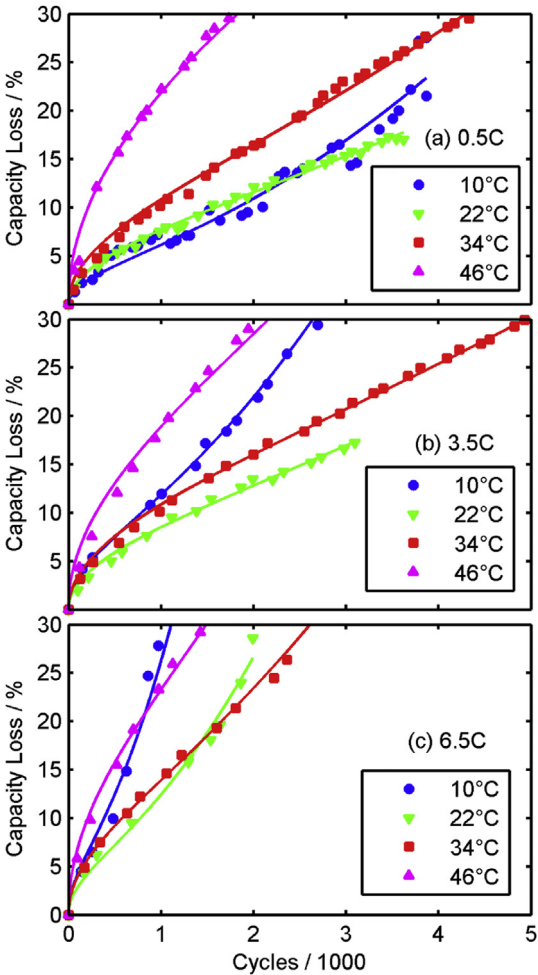

Fig. 2. Capacity loss at four temperatures (10 °C, 22 °C, 34 °C, 46 °C). The panels each correspond to a single rate (0.5 C, 3.5 C, 6.5 C, respectively). The depth of discharge is 50% for all data points in the figure. The x-axis scale is thousands of cycles. Lines shown here are for the guidance of the data trend, not from model fit.

We develop a semi-empirical model that accommodates three important experimental parameters: time, temperature, and discharge rate. We first establish the calendar life model in which the time and temperature dependence of capacity loss were described. The model equation includes a square root of time relation to account for the diffusion-limited capacity loss, while an Arrhenius correlation accounted for the temperature effect. We use the low-rate data at low depth of discharge (DOD) to approximate the calendar life loss. For the cycle life model, we empirically fit the cycle loss with a generalized exponential function that accounts for the rate effects.

In a companion article (Part 2) to this study we build a physics-based model to describe the chemical and mechanical degradation mechanisms, utilizing the experimental insights described in this current article (Part 1).

2. Experimental

2.1. Test matrix

The commercially available 1.5 Ah, 18650 cylindrical cells (UR18650W) were purchased from Sanyo; the cell includes a $LiMn_{1/3}Ni_{1/3}Co_{1/3} + LiMn_2O_4$ positive and graphite negative. They are engineered as high-power-density cells for applications such as power tools, E-bikes and robotics. These lithium-ion cells were tested under the conditions given in the test matrix shown in Fig. 1. Each color-highlighted field represents a cell cycled at that specific condition. Two cells were tested at each of the conditions. These conditions include four different temperatures (10, 22, 34, 46 °C), five levels of DOD (90%, 70%, 50%, 30% and 10%), and five discharges rates (C/2, 2 C, 3.5 C, 5 C and 6.5 C). The 1 C rate corresponds to a current of 1.5 A. The cut-off voltages for the cycle test of all the cells were at 4.2 V and 2.5 V. The constant current charge rates were C/2 for the C/2 discharge rate and 2 C for higher discharge rates. The cells were charged to 4.2 V and held at 4.2 V until the current dropped below 0.075 A for a maximum of 2 days. There was no rest period following the discharge step of each cycle. The constant current charge step commenced immediately following the discharge step.

2.2. Characterization

Prior to cycling tests, each cell was characterized using these four techniques: 1) capacity characterization, 2) relaxation test, 3) electrochemical impedance spectroscopy (EIS), and 4) hybrid pulse power characterization (HPPC). Detailed procedures of each technique are described in the following: 1) For capacity characterization, the cell was fully charged and then discharged at rates of 3 C,
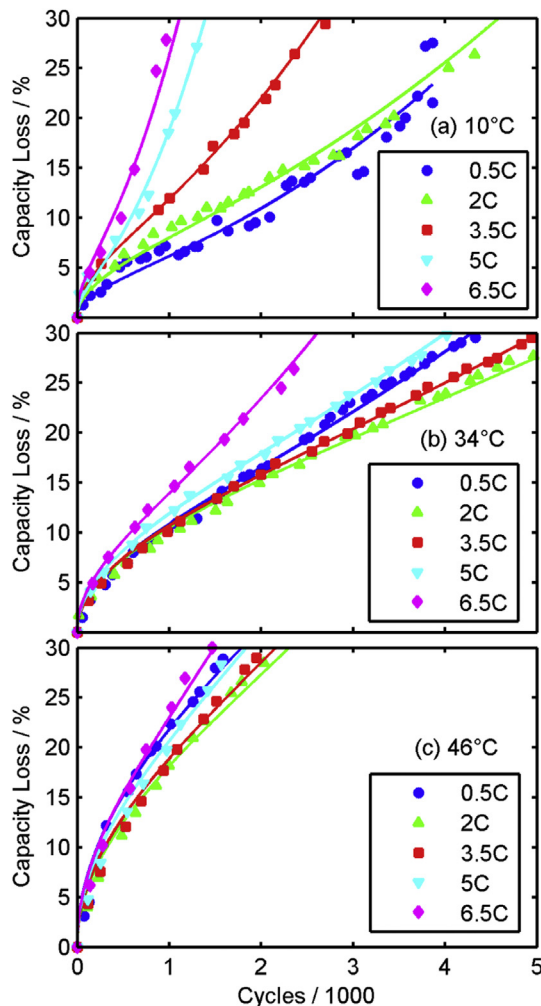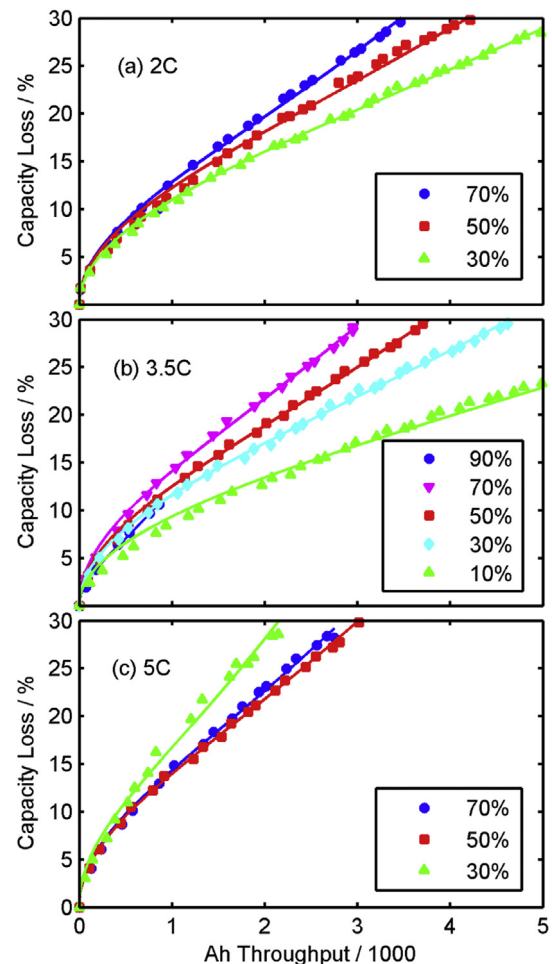

Fig. 3. Capacity loss for a series of discharge rates (0.5 C, 2 C, 3.5 C, 5 C, 6.5 C). The panels each correspond to a single temperature (10 °C, 34 °C and 46 °C, respectively). Depth of discharge is 50% for all data in figure. The x-axis scale is thousands of cycles. Lines shown here are for the guidance of the data trend, not from model fit.

Fig. 4. Capacity loss for a series of discharge depths, at temperature of 34 °C. The three panels each correspond to a discharge current (2 C, 3.5 C, 5 C). Lines shown here are for the guidance of the data trend, not from model fit.

C/2 and C/20. At each rate, two cycles were recorded and the capacity from the second cycle was used as the cell capacity. 2) For the relaxation test, a fully charged cell was discharged for a period of 24 min at C/2 rate, and then followed by a 2 h rest before the subsequent discharge. The test was complete when the discharge voltage reached 2.5 V. 3) The EIS characterization was performed at 50% state of the charge (SOC) which was defined as 72 min of discharge at C/2 rate of a fully charged cell. The EIS measurement was carried out in a frequency range between 0.01 and 100 kHz and AC amplitude of 5 mV. 4) For HPPC characterization, prior to a pulse power sequence, a fully charged cell was discharged to 10% DOD at 1 C rate, and then rested for 1 h. The pulse power sequence was composed of three steps: 1) 5 C discharge for 18 s, 2) rest at OCV for 32 s, and, 3) 3.75 C charge for 10 s. After the pulse sequence, the cell was immediately discharged to 20% DOD and rested for 1 h before the pulse power sequence was repeated. The cell was tested at 10% DOD increments until reaching the cut-off voltage of 2.5 V.

During life cycle tests, cells were stopped every 3rd week for characterization using the procedures described above. The C/2 rate capacity characterization procedures were also performed for every week between cycling test.

For each of the cells tested, the cell capacity measured at a C/2 rate during characterization was used for the subsequent capacity fade quantifications unless otherwise mentioned. The capacity loss was normalized by its initial cell capacity. Most of the cells have reached the defined end of life (EOL) conditions after two years of testing. The EOL is defined as 30% loss of its initial capacity, except that the cells cycled at 90% DOD reached EOL after 10% capacity loss.

The focus of this article is on the capacity measurements of NCM + LMO cells cycled at different conditions. While the relaxation, EIS and HPPC tests provide valuable information on the power performance of the NCM + LMO cells, they are not discussed further in this article.

3. Results and discussion

3.1. Data trends—temperature, rate and DOD effects

Capacity characterization data were used to quantify the capacity fade. Fig. 2 shows the capacity loss as a function of cycle number at four temperatures (10 °C, 22 °C, 34 °C, 46 °C) for three rates (0.5, 3.5, and 6.5 C, respectively). The percent of capacity life loss is plotted as a function of cycle numbers for the cells cycled at 50% DOD. At a low rate (C/2), capacity loss is higher with increasing temperature while at a high rate (6.5 C), both low and high temperatures trigger more capacity loss. These results indicate that two different aging mechanisms contribute to the capacity loss. It is suggested that at a low temperature, due to the slow kinetics of graphite negative electrode, the cycle induced surface cracks on the graphite particles resulted additional SEI formation loss newly formed surfaces is responsible for the capacity fade. At a high temperature, the capacity loss is mainly due to accelerated chemical side reactions that consume lithium, e.g. formation and growth of the solid-electrolyte-interface, SEI. This is explained in more details in later sections. Fig. 3 shows the capacity loss for five discharge rates (0.5 C, 2 C, 3.5 C, 5 C, 6.5 C) at three temperatures
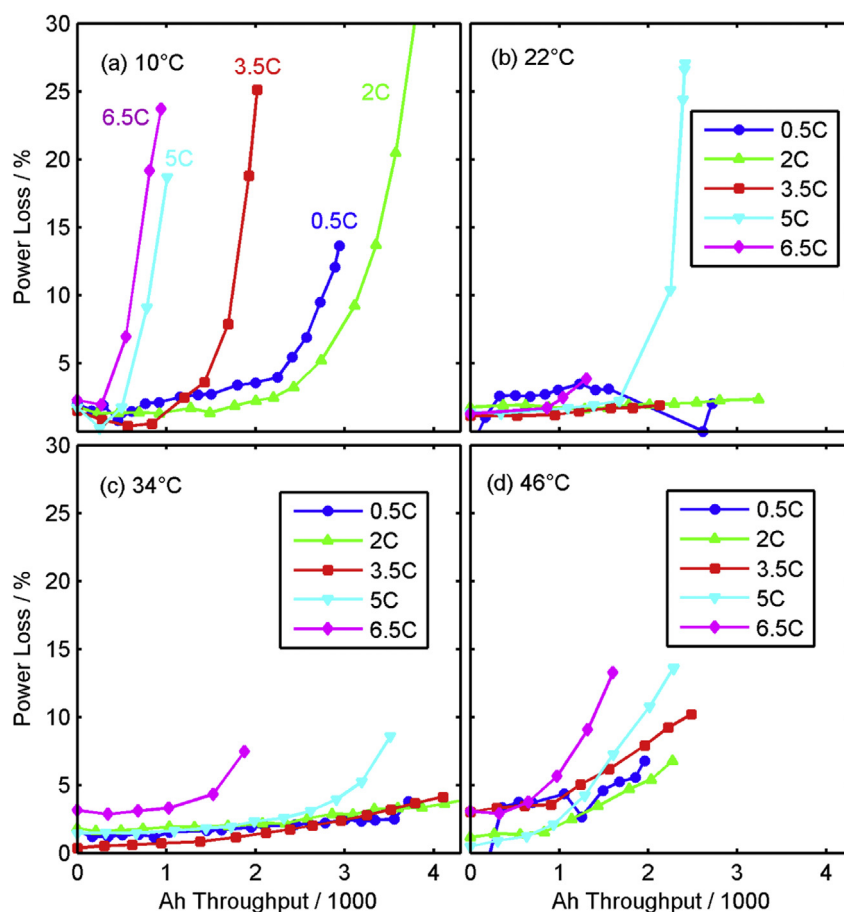

Fig. 5. Power loss, defined as $(Q_{C/20} - Q_{3C})/Q_{C/20}*100$, for a series of discharge rates (0.5 C, 2 C, 3.5 C, 5 C, 6.5 C). The panels each correspond to a single temperature (10 °C, 20 °C, 34 °C and 46 °C, respectively). Depth of discharge is 50% for all data in figure. The x-axis scale is thousands of cycles. Lines shown here are for the guidance of the data trend, not from model fit.
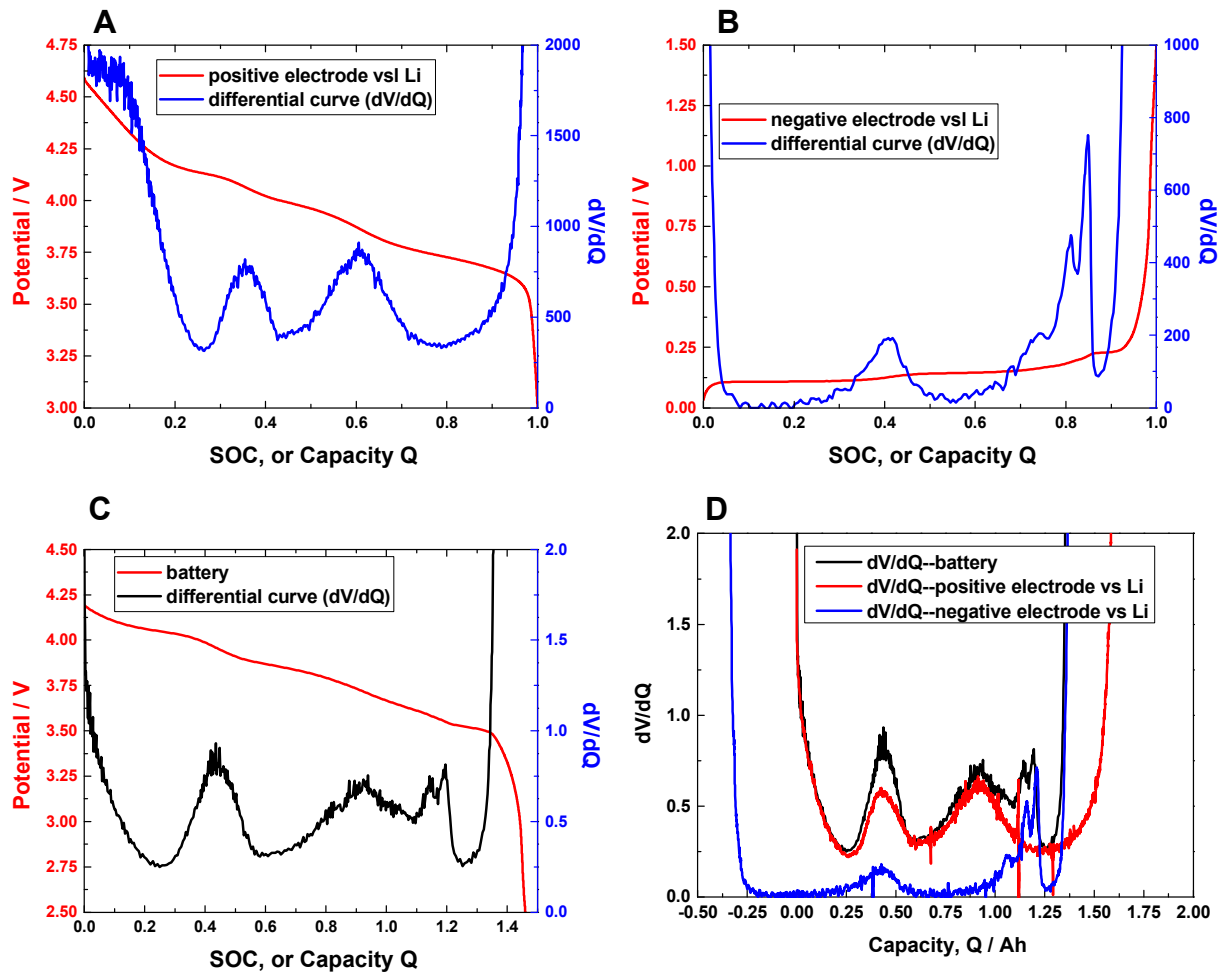
Fig. 6. Voltage profiles and their differential voltage curves plotted as a function of specific capacity. A) positive electrode; B) negative electrode; C) full cell; D) full cell compared with positive and negative electrode.

(10 °C, 34 °C and 46 °C, respectively). At a low temperature of 10 °C, the data trend reveals a clear rate effects indicating that the capacity loss increases with rising discharge rates. At high temperatures, capacity loss tends to be higher for all rates. These results indicate that the temperature effects dominate the capacity loss
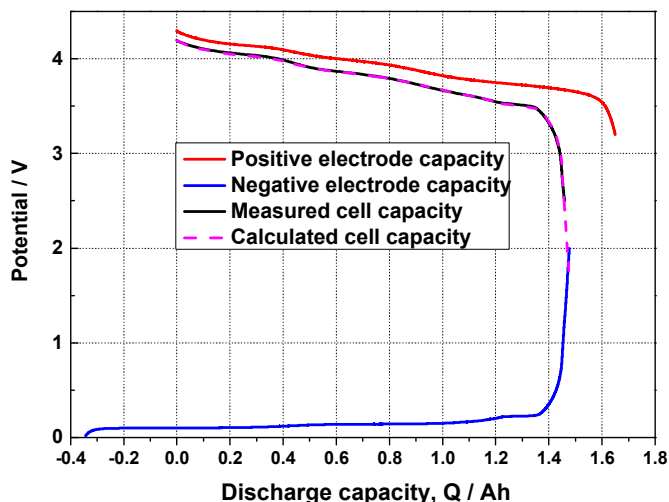

Fig. 7. Deconvolution of a battery discharge voltage profiles.

while rate effects have less impact at higher temperatures. Fig. 4 shows the effects of DOD on capacity loss at three rates (2 C, 3.5 C, and 5 C) at 34 °C temperature. Capacity loss is plotted as a function of Ah-throughput. Ah-throughput represents the amount of charge delivered by the battery during cycling. At each C-rate, Ah-throughput is directly proportional to time; however, the merit of using Ah-throughput is that it allows us to quantify and correlate the capacity fading behaviors for different C-rates. As a general trend, the capacity loss increases at higher DODs. In particular, at 10% DOD, the capacity loss is substantially lower than the cells cycled at higher DODs. On the other hand, the temperature and discharge rate tend to have more significant impacts on capacity fade. At a low temperature, the accelerated loss is observed when the cells are cycled at higher rates. At a low rate, the capacity loss increases with rising temperature. At a high temperature, the accelerated loss is observed at all rates.

We further evaluate the power loss behavior by quantifying the capacity characterization data at different discharge rates. The power loss is defined as the difference in capacity between C/20 and 3 C rates. The disparity in measured capacity between a low and a high rate reflects the kinetics of a cell. Thus, as a battery ages, the difference in capacity values between C/20 and 3 C rates tends to grow due to the resistance rise and slower kinetics. Fig. 5 shows the percent of power loss ratio plotted as a function of Ah throughput for four temperatures (10 °C, 22 °C, 34 °C, 46 °C) and each panel represents a single temperature at five rates (0.5 C, 2 C, 3.5 C, 5 C,
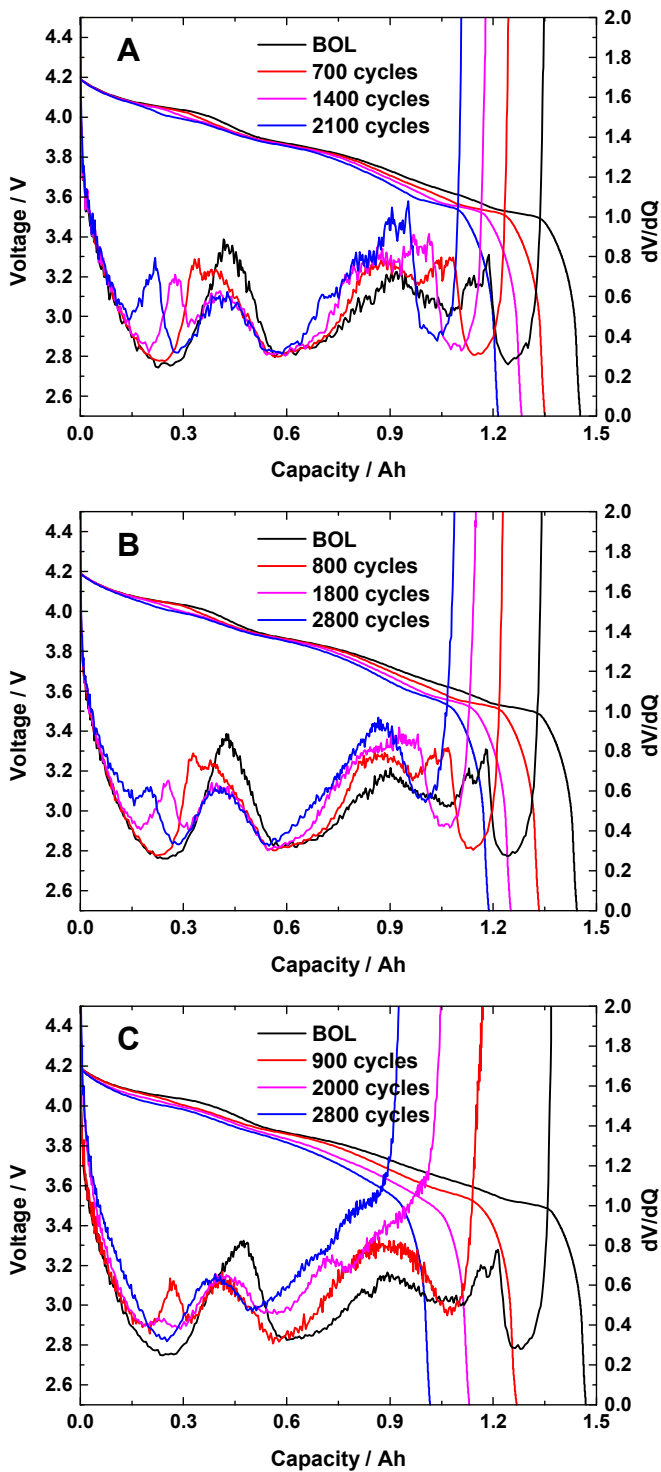
Fig. 8. C/20 discharge profiles and the corresponding differential voltage curves upon cycling at 34 °C and at different rates: A) 0.5 C; B) 3.5 C; and C) 6.5 C.

6.5 C). The percent of power loss ratio is defined as $100(Q_{C/20} - Q_{3C})/Q_{C/20}$, where the difference in capacity values at C/20 and 3 C are normalized respect to C/20 capacity. Power loss can be associated with increased kinetic resistance within the system, which is exacerbated by increased rate of discharge and temperature. For easy comparison, we select the cell conditions cycled at 50% DOD as shown in Fig. 5. For all conditions, the power loss tends to be constant before the onset of an accelerated loss. The power

loss behavior has clear rate dependence; higher discharge rates trigger early onset of the power loss. This effect is particularly evident at the low temperature of 10 °C. At moderate temperatures, accelerated power loss is only observed at very high rates. At a high temperature of 46 °C, the disparities become less visible for different discharge rates. This is consistent with the capacity loss data described, wherein rate effects were less important at high temperatures.

3.2. Aging mechanisms—differential voltage analysis

We further examine the sources of capacity loss by applying differential voltage analysis to identify battery capacity loss mechanisms. This method relies on the unique features from the positive and negative reference profiles. Fig. 6 shows the metal oxide based positive electrode during a lithium insertion process and graphite negative electrode during a lithium extraction process and their corresponding differential voltage curves, respectively. These are the reaction processes occurring during the discharge of a battery cell where lithium ions are moving from the graphite negative to the metal oxide based positive electrode. It is clear that each of the *dV/dQ* curves reveal the distinct features of the active materials. More importantly, the peaks represent the phase transitions of the active materials during lithiation/de-lithiation reactions and the distance between any of the two peaks is directly proportional to the active material capacity or SOC.

The capacities of positive and negative materials can be extracted by comparing the differential voltage curve of the cell with the independently measured differential voltage of the individual electrode curves. As an example, Fig. 6C illustrates the voltage profile of the discharge curve and its derivative at the beginning of life of the battery. The distinctive peaks of the *dV/dQ* curve reveal the signatures from both the positive and negative electrodes. Matching of the peaks from the single electrode curves with respect to the cell allows determination of the capacity of each individual electrode and its SOC position. A graphical representation of this technique is illustrated in Fig. 6D where the positions of the peaks are matched with the single electrode calibration curves. Specifically, the positive electrode differentiation profile from Fig. 6A is allowed to scale on the capacity axis so that its two peaks match the positions of the curves from the cell. The scaling factor is the positive electrode capacity. Similar scaling is performed with the graphite negative electrode and the curve is allowed to shift on the capacity axis, which provides both the negative electrode capacity and the offset between the positive and negative profile. The position of the peaks determines the SOC position and the distance between the peaks of a known electrode material quantifies the active material capacity. As a result, the voltage profile of the cell can be deconvoluted as shown in Fig. 7. The reconstructed cell voltage profile using the fitted positive and negative capacities is in

Table 1

Capacity loss summary of each active component determined using differential voltage technique for selected conditions at 34 °C and three rates: 0.5 C, 3.5 C and 6.5 C.

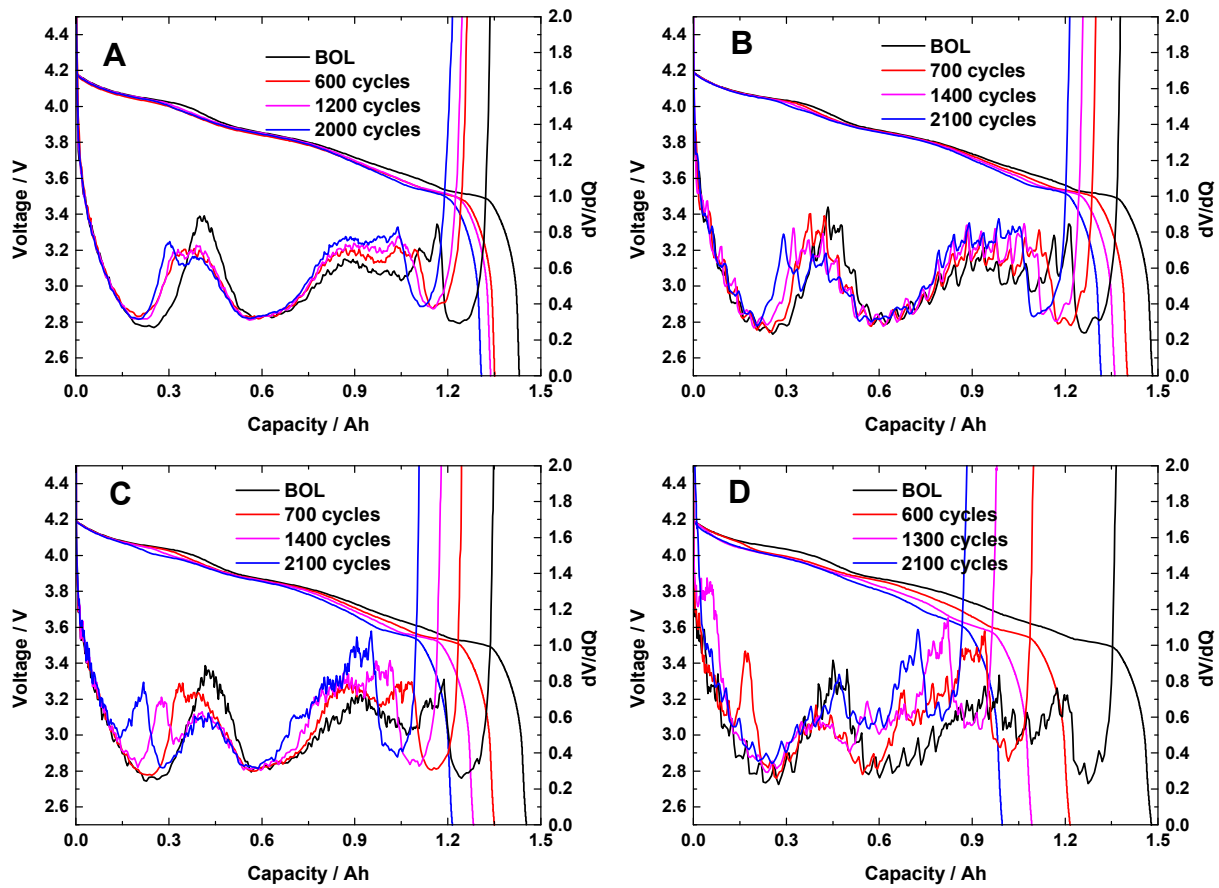| 34 °C			
Rate	0.5 C	3.5 C	6.5 C
Total capacity (lithium) loss (2000 cycles)	17%	17%	30%
Positive electrode capacity loss	8%	7%	12%
Negative electrode capacity loss	4%	6%	17%
Aging mechanism	Lithium loss limiting	Lithium loss limiting	Lithium loss limiting

Fig. 9. C/20 discharge profiles and the corresponding differential voltage curves upon cycling at C/2 cycling condition at four different temperatures: A)10 °C; B) 22 °C; C) 34 °C; and D) 46 °C.

good agreement with the measured values, clarifying the accuracy of this differential voltage technique. In this case, the cell is limited by the amount of active lithium while both positive and negative (host material) capacities are in excess.

As the cell ages, the differential voltage technique enables the quantification of the material loss of each active component in a battery [21,24,26]. To study the rate effects, we select discharge profiles and their corresponding derivative curves of the cell upon cycling for three rates (0.5 C, 3.5 C and 6.5 C) at 34 °C as shown in Fig. 8. Deconvolution of each discharge curve using the differential voltage technique allows yields the capacity fading of each active material in the battery. The leftward shift of the peaks of lithiated graphite indicates the active lithium loss and the shrinking of the distance between the peaks reflects the graphite material loss. At a low rate of C/2, the graphite signatures are well resolved. As the

cycling rate increases, the graphite signature become increasingly less defined, indicative of possible structural change associated with the lithiated graphite staging effects. Nonetheless, based on the distinctive features of the dV/dQ curves, we are able to determine the material loss of each individual electrode (positive electrode, negative electrode, and the amount of lithium). The results of material loss after 2000 cycles are also summarized in Table 1. Graphite material loss is accelerated by high discharge rates, while the positive electrode losses are moderate for all rates. Overall, the loss of active lithium outpaces both the positive and negative

Table 2
Capacity loss summary of each active component determined using differential voltage technique for selected conditions at C/2 rate and four temperatures: 10 °C, 20 °C, 34 °C, and 46 °C.

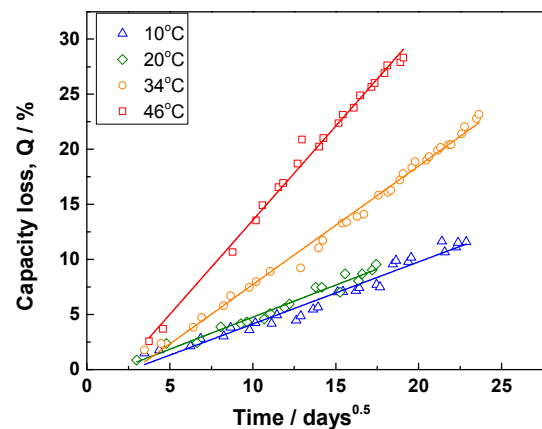| 0.5 C rate				
Temperature	10 °C	20 °C	34 °C	46 °C
Total capacity (lithium) loss (2000 cycles)	8%	11%	17%	22%
Positive electrode capacity loss	4%	4%	8%	11%
Negative electrode capacity loss	1%	3%	4%	5%
Aging mechanism	Lithium loss limiting	Lithium loss limiting	Lithium loss limiting	Lithium loss limiting

Fig. 10. The percentage of capacity loss is plotted as a function of time$^{1/2}$ relation. Linear fits are plotted as the solid lines: (△) 10 °C, (◇) 20 °C, (○) 34 °C, (□) 46 °C. The cycle test conditions were at C/2 rate and 10% DOD.
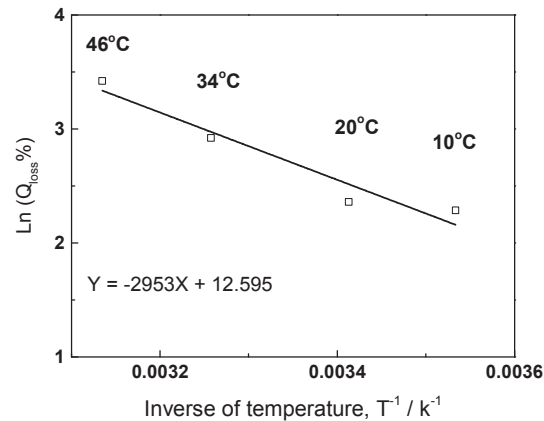
Fig. 11. Inverse temperature dependence of capacity loss is plotted for four different temperatures (10, 20, 34, and 46 °C) after 400 days of testing. The linear fit indicates that the capacity loss behavior follows the Arrhenius law.
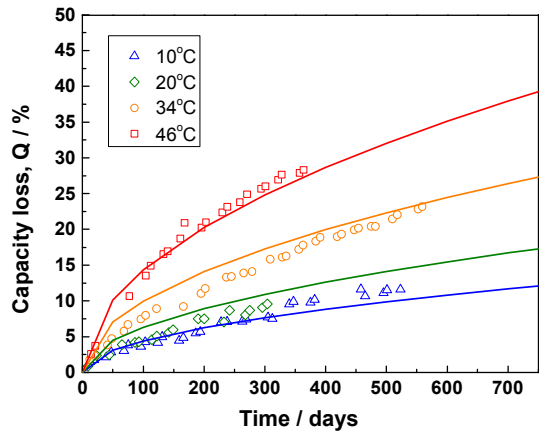

Fig. 12. Simulations of calendar-life prediction model (line) are compared with experimental data (markers) for all four temperatures (10, 20, 34, and 46 °C).
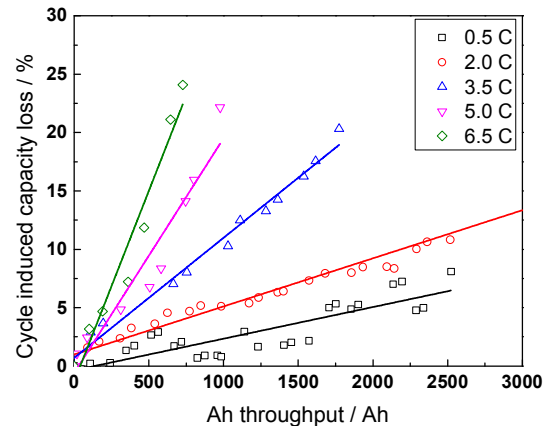

Fig. 13. Cycle life (capacity) loss is plotted as a function of Ah-throughput at 10 °C for 5 different rates: C/2, 2 C, 3.5 C, 5 C, and 6.5 C. Linear fits (lines) were achieved, indicating the capacity loss follows linear trend with Ah throughput or time. Cycle loss is obtained by subtracting the calendar loss from the total capacity loss.
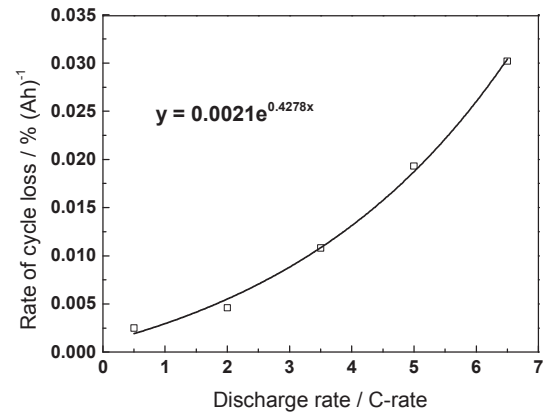

Fig. 14. The rate of cycle loss (slopes from Fig. 13) is plotted as a function of discharge rates at 10 °C. The rate of loss represents well with exponential function.

material losses, indicating the cell capacity is always limited by the amount of useable lithium.

Similarly, we examine the temperature effects on the material loss of each active component in a battery. Fig. 9 shows the discharge profiles and their corresponding derivative curves for four temperatures (10 °C, 22 °C, 34 °C, 46 °C) at C/2 rate. Due to the slow kinetics at low temperatures, the dV/dQ peak features are less well defined. For better accuracy, deconvolution of the discharge curves at each temperature involves the use of pre-determined differential voltage of the individual electrode curves obtained at same temperature. Although the curves in Fig 9B, D are somewhat noisy due to the sampling rates and signal noise of the battery test instruments, it is still possible to accurately identify the dV/dQ peak positions by comparing to the individual electrode potentials. The capacity loss of positive electrode, negative electrode, and the amount of active lithium are quantified (Tables 1 and 2). For easy comparison, the capacity loss results after 2000 cycles are also summarized in Table 2. At all temperatures, the cell capacity is limited by the amount of active lithium, whereas lithium loss always outpaces both the positive and negative material loss. All active material loss (positive electrode, negative electrode, and the amount of lithium) tend to increase with temperature. While moderate losses are observed for the positive electrode, the loss of negative electrode material remains minimal at a C/2 cycling rate.

The positive electrode contains a physical mixture of LMO and NCM materials. Losses of this composite postive electrode material were apparent in the differential voltage analysis, but they were not the capacity limiting factor for any of the test conditions in Tables 1 and 2. The presence of LMO is generally known to accelarate the SEI growth on the anode due to the dissolution and cross-over of Mn^{3+} ions. While commercial cells are likely include strategies to mitigate this effect, such as SEI additives, cell balancing and particle coating, it is still likely to be an important factor.

Table 3
Summary of model equations accounts for both cycle life and calendar life.

	Cycle life model	Calendar life model
10 °C	[0.0021exp(0.4278·rate)]·Ah$_{throughput}$	14,876 (days)$^{0.5}$·exp(-24.5 kJ/RT)
20 °C	[0.0008exp(0.3903·rate)]·Ah$_{throughput}$	
34 °C	[0.0010exp(0.3107·rate)]·Ah$_{throughput}$	
46 °C	[0.0045exp(0.1826·rate)]·Ah$_{throughput}$	

3.3. Modeling calendar life

The large test matrix, including time, temperature, DOD and rate, allows statistical evaluation of the parameters effecting battery life and provides sufficient data for model development. Using capacity characterization data, the cycle-number-dependent capacity loss data were used to quantify the capacity loss rate for the life model development.

Calendar life performance is a direct representation of irreversible self-discharge capacity loss. This capacity fade is mainly due the lithium inventory loss during solid-state-interphase (SEI) formation at the graphite negative electrode [27,28]. The growth of SEI layer consumes lithium that causes irreversible capacity loss. It is known that this SEI growth is diffusion limited process, indicating the capacity loss follows time$^{1/2}$ relationship [11,16,17,27–30]. SEI formation is also a thermally activated process that can be simulated with an Arrhenius law dependence on temperature [11,29,30]. Thus, the calendar life is strongly affected by two parameters: time (t) and temperature (T). In this case, we adopt a simplified battery calendar life equation to account for Arrhenius type temperature dependence and diffusion-controlled lithium corrosion reaction, $t^{0.5}$ relation [27,28,31,32]:

$$Q_{loss,\%} = A \cdot \exp\left(-E_a/RT\right) t^{0.5} \tag{1}$$

In Equation (1), Q_{loss}, is the percentage of capacity loss, A is the pre-exponential factor, E_a is the activation energy in J mol^{-1}, R is the gas constant, T is the absolute temperature. For analytical purposes, we rearrange this slightly to.

$$\ln\left(Q_{loss,\%}\right) = \ln\left(At^{0.5}\right) - \left(E_a/RT\right) \tag{2}$$

Calendar loss rates are typically obtained by studying the capacity loss of Li-ion cells stored at constant voltage or open circuit. However, the test matrix for this study did not include stored NCM + LMO cells. In Fig. 2, it can be seen that the test condition that are closest to storage (i.e., the mildest cycling conditions) are the low-rate (C/2) and shallow DOD (10%) cycling conditions. We used the cells tested at these conditions as the baseline values to approximate the calendar loss. . In Fig. 10, the percentage of capacity loss at these mild cycling conditions is plotted as a function of days$^{0.5}$ at 10, 20, 34 and 46 °C for the cells cycled at 10% DOD at C/2 rate. The lines represent the linear fit at each temperature. This t$^{1/2}$ relationship further indicates the calendar loss is a diffusion-controlled process, consistent with our described assumption. Thus, according to Equation (1), the slope of the each line at each of the temperatures reflects the temperature-dependent capacity loss.

Equation (2) was used to extract the fitting parameters for the calendar life model. We can determine all the parameter values using a single step optimization process when plotting a logarithmic percentage of capacity loss as a function of inverse temperature (1/T). Fig. 11 shows an example where the log of capacity percent loss is plotted as a function of 1/T for the losses after 400 days. The line represents a linear fit of the temperature-dependent capacity loss. According to Equation (2), the slope of the line represents $-E_a/R$, while the intercept equals to ln($At^{0.5}$). As a result, the capacity loss calendar life is expressed as:

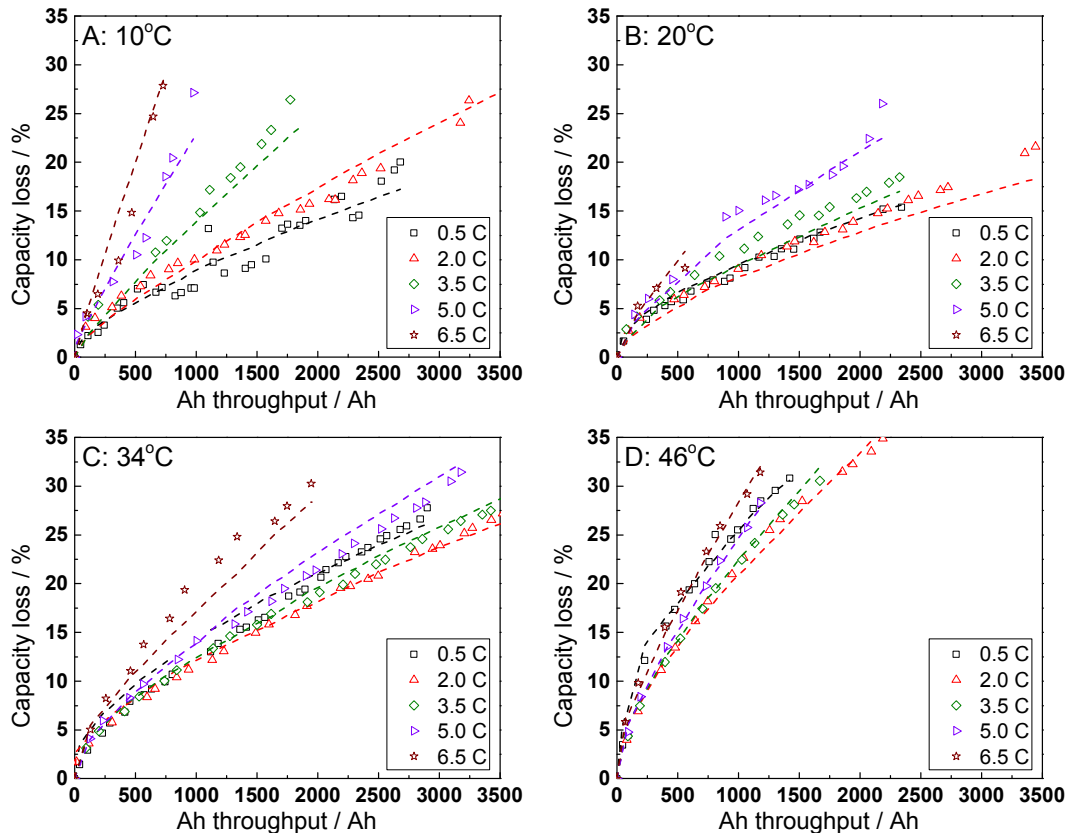$$\left(Q_{loss}\right) = 14876 \cdot \exp\left(-24.5kJ/RT\right) \cdot days^{0.5} \tag{3}$$

Fig. 15. Simulations of combined calendar-life and cycle-life prediction model (line) are compared with experimental data (markers) for four temperatures (10, 20, 34, and 46 °C), five rates (C/2, 2 C, 3.5 C, 5 C, and 6.5 C rate) and at 50%DOD.

Using the calendar life model in Equation (3), we are able to simulate the capacity fade under various conditions. In Fig. 12, simulations of the capacity fade at different temperatures are compared with the experimental data. These results further demonstrate that for calendar life, the time and temperature are the two parameters that strongly impact capacity fade. As an open question, this model has ignored the calendar life effect due to the end-of-charge-voltage, EOCV. In the prior reports, [17,31] the results indicate that the calendar life has EOCV dependence which we did not consider in our model. By choosing the 10%DOD data for the calendar life modeling, we also assume that the shallow DOD cycling at a slow rate has minimal impact on capacity loss.

3.4. Modeling cycle life

For the simplified approach we are employing, once the calendar life loss is known, quantifying the cycle life loss is very straightforward. We choose all the conditions from 50% DOD cycle data for fitting the model. The cycle life loss is calculated using the total loss measured from the cycle data minus the calendar life loss from the model. As an example, Fig. 13 shows the percent of cycle life loss as a function of Ah throughput for all rates at 10 °C temperature. The lines in Fig. 13 represent the linear fit of the cycle life data at each of the rates. These results also agree with the prior findings [28,32,33] that the cycle life loss follows a linear trend with time. The slope of the lines represents the rate of cycle induced loss at each of the C-rates. To build an empirical correlation for the rate effects, we consider the rate of cycle loss (the slope) plotted as a function of the C-rate, as shown in Fig. 14. The rate effect is fitted by an exponential function. Thus the function form of the cycle life model is.

$$Q_{loss,\%} = B_1 \cdot \exp\left(B_2 \cdot \text{rate}\right) \cdot \text{Ah}_{\text{throughput}} \tag{4}$$

The fitted results for all temperatures are summarized in Table 3. Simulation results of the combined cycle life models and calendar life model are compared with the measured total capacity loss data for all temperatures in Fig. 15. (In contrast, Fig. 13 shows only the cycle loss). The model projections are consistent with the experimental data for all the conditions.

To further understand the temperature dependence on cycle life, we plotted the pre-exponential factor B_1, and the exponential factor B_2 as a function of temperature (Fig. 16). It appears that there is a general linear trend for the exponential factor B_2 to decrease with increasing temperature. The pre-exponential coefficients, B_1, on the other hand, are higher at both 10 and 46 °C. While the root causes for large cycle life loss at 46 °C is remain largely unknown, it seems that the lithium side reactions with solvent is enhanced by higher temperatures above and beyond what the calendar life portion captures. A fairly good empirical fit was achieved using a second order polynomial relation. From the empirical fitting of the pre-exponential factor B_1, and the exponential factor B_2, we are able to build a single equation to predict battery life that accounts for various temperature and rates. The function form of this generalized equation is

$$Q_{loss,\%} = \left(a \cdot T^2 + b \cdot T + c\right)\exp\left[\left(d \cdot T + e\right) \cdot I_{\text{rate}}\right] \cdot \text{Ah}_{\text{throughput}}$$
$$+ f \cdot t^{0.5} \cdot \exp\left[-E_a/RT\right]$$
$$\tag{5}$$

Coefficient values and units			
a	8.61E-6, 1/Ah-K^2	I_{rate}	C-rate
b	−5.13E-3, 1/Ah-K	t	Days
c	7.63E-1, 1/Ah	E_a	24.5, kJ mol^{-1}
d	−6.7E-3, 1/K-(C-rate)	R	8.314, J mol^{-1} K^{-1}
e	2.35, 1/(C-rate)	T	K
f	14,876, 1/day$^{1/2}$		

Using the generalized life model in Equation (5), we are able to simulate the capacity fade under various temperatures and rates. In Fig. 17, predicted capacity fade are plotted against the experimental measured capacity loss for all 50%DOD conditions and all rates at each of the temperatures. The black diagonal line represents 45° line where the predicted losses are equal to the actual losses those were measured experimentally. The results indicated that the model is slightly under-predict the modest temperature of 20 °C and over-predict the higher temperatures at 34 and 46 °C. For the most of the conditions, predicted values are within ±5% capacity loss of the measured values. Overall, we are able to build a life
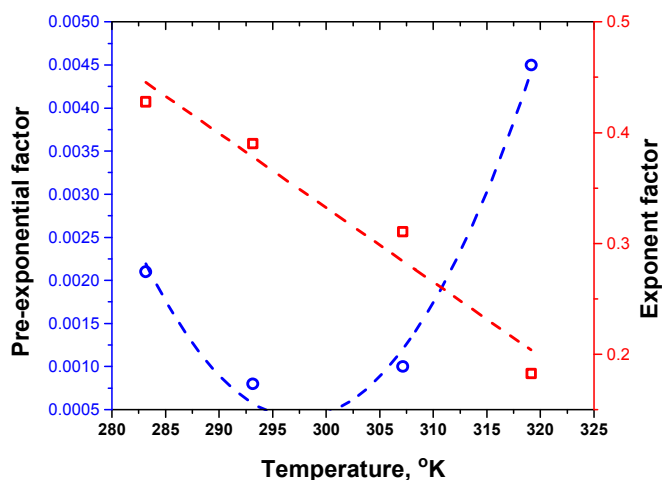

Fig. 16. The pre-exponential factor B_1, and the exponential factor B_2 of Equation (4) is plotted as a function of temperature. The red lines represents the linear fit of the exponential factor and blue line represents the second order polynomial fit of the pre-exponential factor. (For interpretation of the references to color in this figure legend, the reader is referred to the web version of this article.)
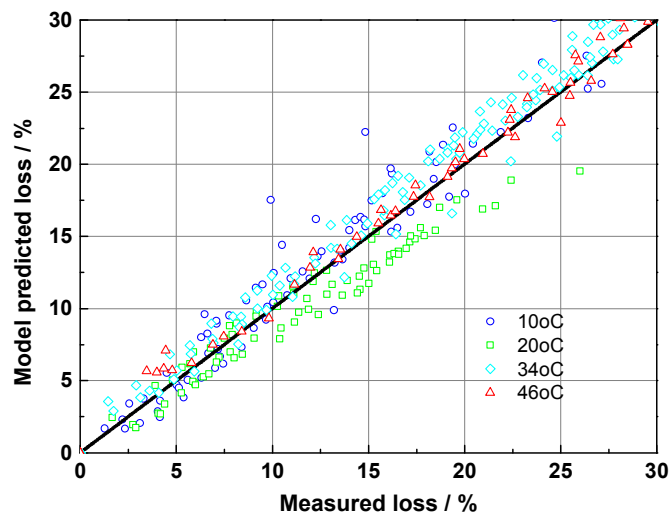

Fig. 17. Simulation of combined calendar-life and cycle-life losses are plotted against the experimental data for four temperatures ((◊) 10, (□) 20, (○) 34, and (△) 46 °C) for all rates at 50%DOD. The diagonal line (black) represents the 45° line where the predicted values are equal to the measured values.
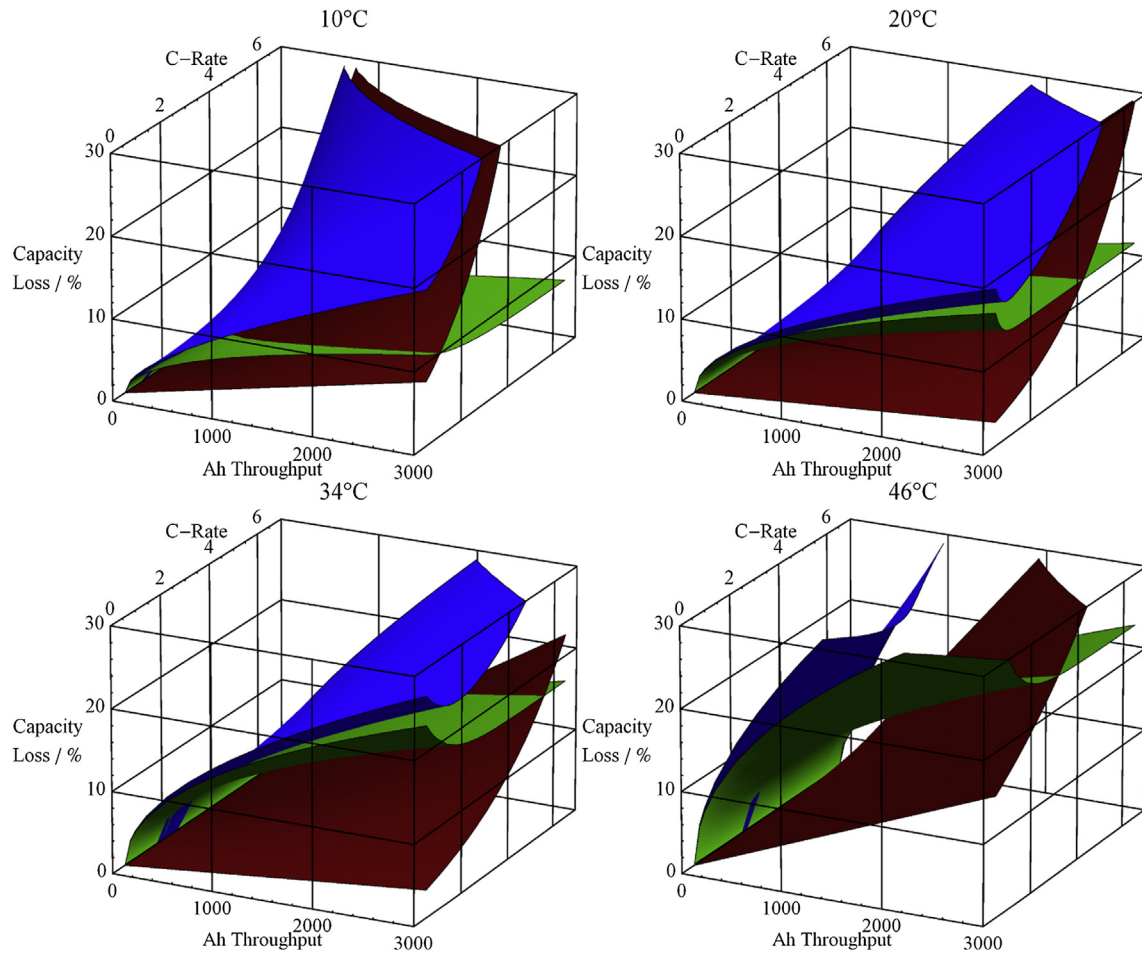
Fig. 18. Simulation of calendar life model and cycle life model as a function of discharge rate and Ah throughput for all four temperatures: 10, 20, 34, and 46 °C. (blue: total life loss; green: calendar life loss; and red: cycle life loss). (For interpretation of the references to color in this figure legend, the reader is referred to the web version of this article.)

model correlation that able to represent the capacity loss under various temperature and rates. More importantly, the decoupling of calendar life and cycle life provides important insights relative to the aging mechanisms responsible for the capacity fade. Fig. 18 shows graphical representations of the calendar loss and cycle loss plotted separately for all temperatures. It is clear that at low temperatures (e.g. 10 °C), the cycle-life loss dominates at higher rates of discharge.

As described in greater detail in Part 2 of this study, [34] this observation can be explained in terms of diffusion-induced-stresses that occur in the graphite negative electrode during fast discharge. High rates produce higher diffusion induced stress fields and trigger cracks on the graphite particles. Consequently, the growth of the SEI layer on the cracked surfaces consumes the active lithium on subsequent charge, which is responsible for the capacity loss. The impact due to the rate effects becomes more evident when the lithium diffusion kinetics in graphite negative are hindered at low temperatures. Cycle-life loss decreases with increasing temperatures. On the other hand, at higher temperatures, the calendar life effect dominates. This is mainly attributed to the increase in the kinetics of the chemical processes for the undesired side reactions (e.g. lithium corrosion for SEI formation). Decoupling of the cycle-life loss and calendar-life loss simplifies the examination of the two different aging mechanisms responsible for the capacity fade: chemical induced degradation and mechanical induced degradations. While high temperatures trigger more calendar-life loss

(chemical degradation), low temperatures and high rates induce more cycle-life loss (mechanical degradation).

References

[1] J. Christensen, J. Newman, J. Solid State Electrochem. 10 (5) (2006) 293–319.
[2] M. Dubarry, B.Y. Liaw, J. Power Sources 174 (2) (2007) 856–860.
[3] C. Fellner, J. Newman, J. Power Sources 85 (2) (2000) 229–236.
[4] T.F. Fuller, M. Doyle, J. Newman, J. Electrochem. Soc. 141 (1) (1994) 1–10.
[5] P.M. Gomadam, J.W. Weidner, R.A. Dougal, R.E. White, Mathematical Modeling of Lithium-ion and Nickel Battery Systems, Elsevier Science BV, 2002.
[6] B.Y. Liaw, R.G. Jungst, G. Nagasubramanian, H.L. Case, D.H. Doughty, J. Power Sources 140 (1) (2005) 157–161.
[7] G. Ning, B.N. Popov, J. Electrochem. Soc. 151 (10) (2004) A1584–A1591.
[8] P. Ramadass, B. Haran, P.M. Gomadam, R. White, B.N. Popov, J. Electrochem. Soc. 151 (2) (2004) A196–A203.
[9] M. Safari, M. Morcrette, A. Teyssot, C. Delacourt, J. Electrochem. Soc. 156 (3) (2009) A145–A153.
[10] S. Santhanagopalan, Q.Z. Guo, P. Ramadass, R.E. White, J. Power Sources 156 (2) (2006) 620–628.
[11] R. Spotnitz, J. Power Sources 113 (1) (2003) 72–80.
[12] B. Wu, M. Mohammed, D. Brigham, R. Elder, R.E. White, J. Power Sources 101 (2) (2001) 149–157.
[13] R. Darling, J. Newman, J. Electrochem. Soc. 145 (3) (1998) 990–998.
[14] J. Christensen, J. Newman, J. Electrochem. Soc. 150 (11) (2003) A1416–A1420.
[15] I. Bloom, S.A. Jones, E.G. Polzin, V.S. Battaglia, G.L. Henriksen, C.G. Motloch, R.B. Wright, R.G. Jungst, H.L. Case, D.H. Doughty, J. Power Sources 111 (1) (2002) 152–159.
[16] R.B. Wright, J.P. Christophersen, C.G. Motloch, J.R. Belt, C.D. Ho, V.S. Battaglia, J.A. Barnes, T.Q. Duong, R.A. Sutula, J. Power Sources 119 (Sp. Iss. SI) (2003) 865–869.
[17] R.B. Wright, C.G. Motloch, J.R. Belt, J.P. Christophersen, C.D. Ho, R.A. Richardson, I. Bloom, S.A. Jones, V.S. Battaglia, G.L. Henriksen,

T. Unkelhaeuser, D. Ingersoll, H.L. Case, S.A. Rogers, R.A. Sutula, J. Power Sources 110 (2) (2002) 445—470.

[18] J. Wang, P. Liu, J. Hicks-Garner, E. Sherman, S. Soukiazian, M. Verbrugge, H. Tataria, J. Musser, P. Finamore, J. Power Sources 196 (8) (2011) 3942—3948.

[19] J.W. Fergus, J. Power Sources 195 (4) (2010) 939—954.

[20] H. Kitao, T. Fujihara, K. Takeda, N. Nakanishi, T. Nohma, Electrochem. Solid-State Lett. 8 (2) (2005) A87—A90.

[21] A.J. Smith, J.C. Burns, D. Xiong, J.R. Dahn, J. Electrochem. Soc. 158 (10) (2011) A1136—A1142.

[22] A.J. Smith, S.R. Smith, T. Byrne, J.C. Burns, J.R. Dahn, J. Electrochem. Soc. 159 (10) (2012) A1696—A1701.

[23] M. Dubarry, C. Truchot, M. Cugnet, B.Y. Liaw, K. Gering, S. Sazhin, D. Jamison, C. Michelbacher, J. Power Sources 196 (23) (2011) 10328—10335.

[24] M. Dubarry, C. Truchot, B.Y. Liaw, K. Gering, S. Sazhin, D. Jamison, C. Michelbacher, J. Power Sources 196 (23) (2011) 10336—10343.

[25] K.L. Gering, S.V. Sazhin, D.K. Jamison, C.J. Michelbacher, B.Y. Liaw, M. Dubarry, M. Cugnet, J. Power Sources 196 (7) (2011) 3395—3403.

[26] A.J. Smith, H.M. Dahn, J.C. Burns, J.R. Dahn, J. Electrochem. Soc. 159 (6) (2012) A705—A710.

[27] H. Ploehn, P. Ramadass, R. White, J. Electrochem. Soc. 151 (3) (2004) A456—A462.

[28] K. Smith, M. Earleywin, E. Wood, J. Neubauer, A. Pesaran, in: 7th Lithium Battery Power Conference, Las Vegas, NV, November 7—8, 2011. Las Vegas, NV.

[29] M. Broussely, P. Biensan, F. Bonhomme, P. Blanchard, S. Herreyre, K. Nechev, R.J. Staniewicz, J. Power Sources 146 (2005) 90—96.

[30] M. Broussely, S. Herreyre, P. Biensan, P. Kasztejna, K. Nechev, R.J. Staniewicz, J. Power Sources 97-8 (2001) 13—21.

[31] I. Bloom, B.W. Cole, J.J. Sohn, S.A. Jones, E.G. Polzin, V.S. Battaglia, G.L. Henriksen, C. Motloch, R. Richardson, T. Unkelhaeuser, D. Ingersoll, H.L. Case, J. Power Sources 101 (2) (2001) 238—247.

[32] K. Smith, M. Earleywine, E. Wood, J. Neubauer, A. Pesaran, Comparison of Plug-in Hybrid Electric Vehicle Battery Life across Geographies and Drive Cycles, 2012. SAE Technical Papers.

[33] K. Smith, T. Markel, A. Pesaran, in: 26th International Battery Seminar & Exhibit, 2009. Fort lauderdale, FL.

[34] R. Deshpande, M. Verbrugge, Y.T. Cheng, J. Wang, P. Liu, J. Electrochem. Soc. 159 (10) (2012) A1730—A1738.